Intense Surface Winds from Gravity Wave Breaking in Simulations of a Destructive Macroburst

RUSS S. SCHUMACHER,[a] SAMUEL J. CHILDS,[a] AND REBECCA D. ADAMS-SELIN[b]

[a] *Department of Atmospheric Science, Colorado State University, Fort Collins, Colorado*
[b] *Verisk Atmospheric and Environmental Research, Bellevue, Nebraska*

(Manuscript received 7 April 2022, in final form 7 December 2022)

ABSTRACT: Shortly after 0600 UTC (midnight local time) 9 June 2020, a convective line produced severe winds across parts of northeast Colorado that caused extensive damage, especially in the town of Akron. High-resolution observations showed gusts exceeding 50 m s^{-1}, accompanied by extremely large pressure fluctuations, including a 5-hPa pressure surge in 19 s immediately following the strongest winds and a 15-hPa pressure drop in the following 3 min. Numerical simulations of this event (using the WRF Model) and with horizontally homogeneous initial conditions (using Cloud Model 1) reveal that the severe winds in this event were associated with gravity wave dynamics. In a very stable postfrontal environment, elevated convection initiated and led to a long-lived gravity wave. Strong low-level vertical wind shear supported the amplification and eventual breaking of this wave, resulting in at least two sequential strong downbursts. This wave-breaking mechanism is different from the usual downburst mechanism associated with negative buoyancy resulting from latent cooling. The model output reproduces key features of the high-resolution observations, including similar convective structures, large temperature and pressure fluctuations, and intense near-surface wind speeds. The findings of this study reveal a series of previously unexplored mesoscale and storm-scale processes that can result in destructive winds.

SIGNIFICANCE STATEMENT: Downbursts of intense wind can produce significant damage, as was the case on 9 June 2020 in Akron, Colorado. Past research on downbursts has shown that they occur when raindrops, graupel, and hail in thunderstorms evaporate and melt, cooling the air and causing it to sink rapidly. In this research, we used numerical models of the atmosphere, along with high-resolution observations, to show that the Akron downburst was different. Unlike typical lines of thunderstorms, those responsible for the Akron macroburst produced a wave in the atmosphere, which broke, resulting in rapidly sinking air and severe surface winds.

KEYWORDS: Gravity waves; Wave breaking; Downbursts; Severe storms; Mesoscale models

1. Introduction

A destructive macroburst impacted the town of Akron, Colorado, just after 0600 UTC [midnight mountain daylight time (MDT)] 9 June 2020, resulting in widespread power outages and substantial damage to buildings, vehicles, and vegetation. Near-surface wind gusts were recorded as high as 37.04 m s^{-1} at the Automated Surface Observing Station (ASOS) in Akron and 50.45 m s^{-1} at a 10-m tower at the U.S. Department of Agriculture (USDA) research site east of the town, the latter of which became the highest convective wind gust in Colorado state history per the Storm Prediction Center (SPC) data archives dating to 1955. Moreover, an Eddy-Covariance (EC) tower at the USDA site recorded a 51.12 m s^{-1} instantaneous wind speed at 2.3 m AGL and 10-Hz resolution. At least five other surface stations throughout northeastern Colorado measured wind gusts in excess of 35 m s^{-1} associated with the storm of interest, affirming its macroburst designation. Childs et al. (2021) investigated the unique observed patterns of surface pressure, temperature, wind speed, and wind direction at extremely high temporal resolution. Their major findings that serve as motivation for the work presented here can be summarized as follows:

1) The Akron macroburst storm was one of several short lines of convection on this night extending from northeastern Colorado through central Nebraska. While most of these convective lines were oriented north–south in a wavelike pattern, the Akron storm suddenly elongated in the east–west direction prior to producing extreme downburst winds (Fig. 1).
2) A National Weather Service (NWS) storm survey revealed damage patterns consistent with both radial outflow—characteristic of a downburst—and straight-line winds indicative of an outflow boundary. The damage was consistent with an EF1 rating (National Weather Service 2020).
3) High-resolution surface observations revealed rapid oscillations in both pressure and temperature not seen in previous downburst literature. Noteworthy was a pressure surge of about 6 hPa in around 10 min [not shown; see Fig. 13 of Childs et al. (2021)], followed by a further

Supplemental information related to this paper is available at the Journals Online website: https://doi.org/10.1175/MWR-D-22-0103.s1.

Childs's current affiliation: U.S. Air Force, Wright-Patterson AFB, Ohio.

Corresponding author: Russ Schumacher, russ.schumacher@colostate.edu

DOI: 10.1175/MWR-D-22-0103.1

© 2023 American Meteorological Society. For information regarding reuse of this content and general copyright information, consult the AMS Copyright Policy (www.ametsoc.org/PUBSReuseLicenses).

Brought to you by Colorado State University Libraries | Unauthenticated | Downloaded 03/10/23 07:13 PM UTC

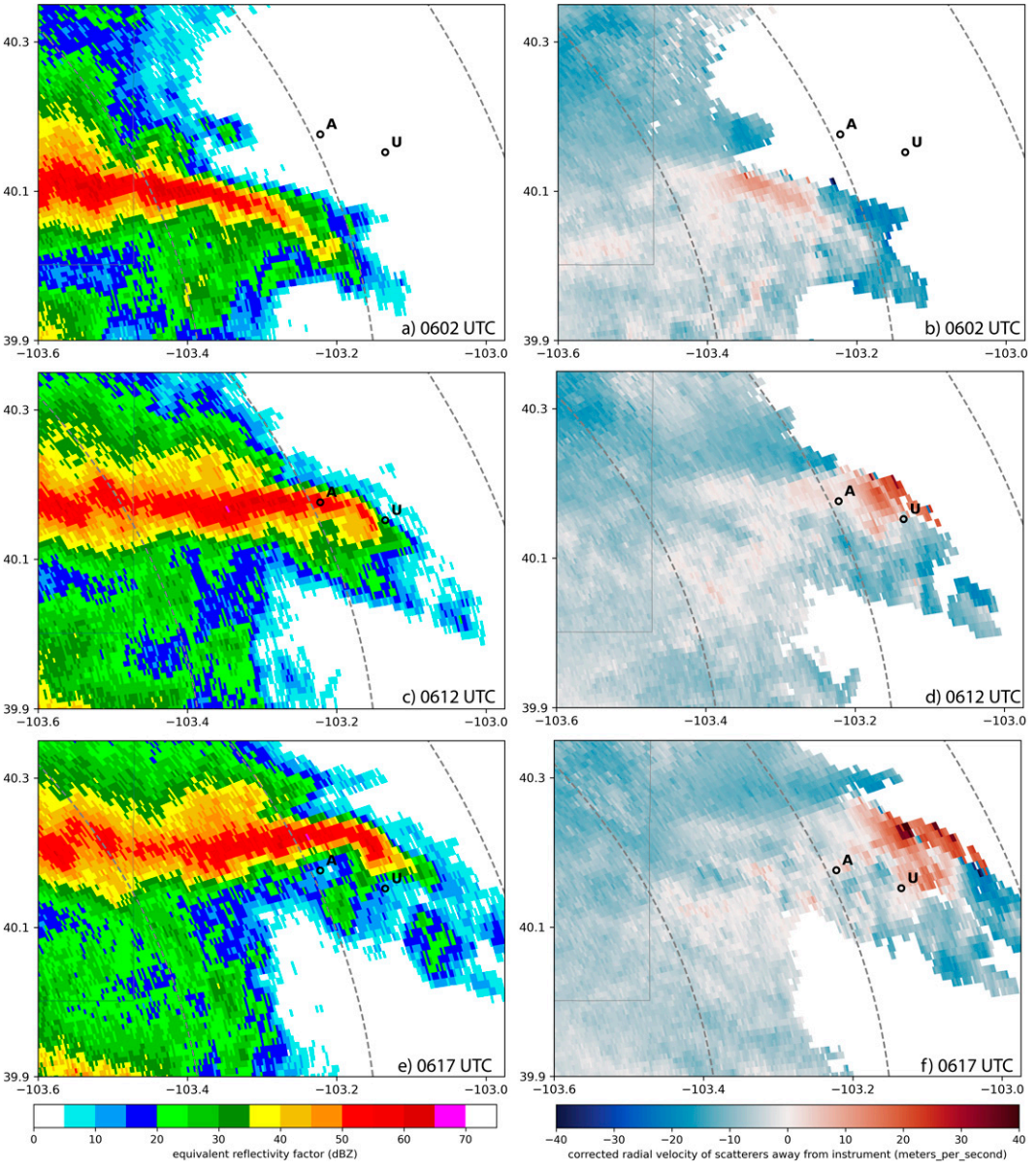

FIG. 1. (a),(c),(e) Radar reflectivity factor (dBZ) and (b),(d),(f) radial velocity from the Denver, Colorado, WSR-88D (KFTG) at (a),(b) 0602; (c),(d) 0612; and (e),(f) 0617 UTC 9 Jun 2020. The two open black circles represent the locations of KAKO (A) and USDA towers (U). The elevation angle shown is 0.5°, and range rings are shown at 100, 120, and 140 km. The velocities in (b), (d), and (f) were dealiased using the region-based method from the Py-ART package (Helmus and Collis 2016). From Childs et al. (2021).

5-hPa pressure surge immediately prior to the maximum wind gusts and concurrent with a 1°–2°C temperature spike that is not typical of past downburst observations (Fig. 2).

4) Analysis soundings showed moist low levels and a steep temperature inversion. The vertical profile of Scorer parameter showed potential for trapped gravity waves.
5) A 4-km Weather Research and Forecasting (WRF) forecast, as well as the High-Resolution Rapid Refresh (HRRR) model, were able to capture wavelike convective structures 6 h in advance, albeit with slight timing and location errors and underestimates of the observed wind maxima.

This study will expand upon the observational findings of Childs et al. (2021) by conducting and analyzing numerical simulations, with a goal of better understanding the physical processes at work in the 9 June 2020 event.

Previous modeling studies of damaging wind events that are spatially and/or temporally smaller than derechos or bow echoes (Johns and Hirt 1987) have almost entirely focused on

Brought to you by Colorado State University Libraries | Unauthenticated | Downloaded 03/10/23 07:13 PM UTC

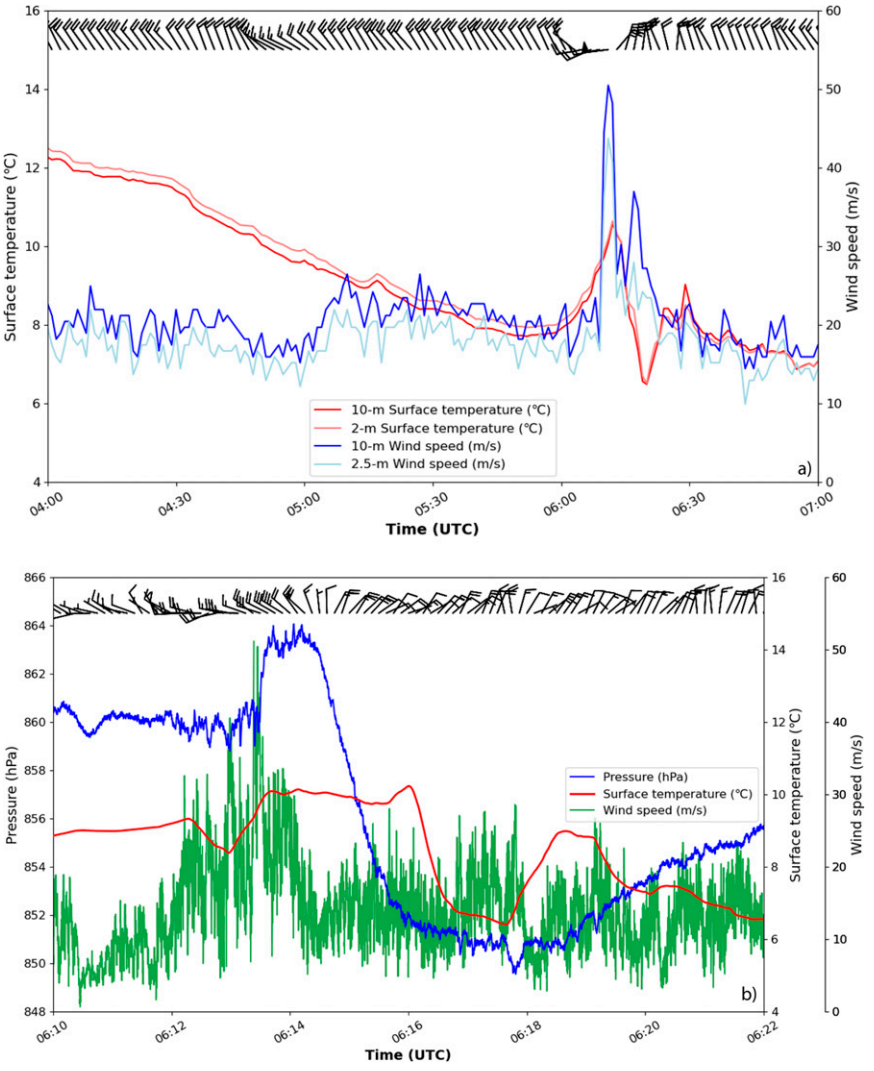

FIG. 2. (a) Time series of surface temperature at 10 and 2 m (°C), and wind speed at 10 and 2.5 m (m s^{-1}) from a 10-m tower on 9 Jun 2020. Data frequency is every minute, and wind speed represents the maximum gust from a sampling frequency of 5 s. (b) Time series of surface temperature at 2.3 m AGL (°C), station pressure (hPa), and instantaneous wind speed (m s^{-1}) from an eddy covariance tower, focused on the time of the macroburst. Temperature is plotted every millisecond (10-Hz frequency), pressure is plotted every 10 s, and wind speed is plotted every second. In both panels, wind pennants represent 50 m s^{-1}, full barbs 10 m s^{-1}, and half barbs 5 m s^{-1}. Adapted from Childs et al. (2021).

microbursts. Given the extensive computational resources needed to simulate the complex processes at such small scales, initial work used one-dimensional simulations. Downdrafts were simulated by imposing a precipitation size distribution entering the top of a column (e.g., Srivastava 1985, 1987), revealing downdraft sensitivity to precipitation phase and size distribution as well as the environmental temperature and humidity profiles. The cooling due to melting of hail or graupel was key to initiating the downdraft; evaporative cooling of rain helped intensify its motion once generated; precipitation loading had varying levels of impact depending on the study (Hjelmfelt 1988; Atlas et al. 2004). As computational resources advanced, idealized simulations expanded to two and three dimensions allowing the downburst structure and its environmental interaction to be simulated (Proctor 1988, 1989) even in simulations with partially resolved turbulent processes (Anabor et al. 2011). The expanding outflow from the downdraft was found to take the form of a ring vortex with depths generally smaller than circulations associated with a gust front (Proctor 1988, 1993; Wakimoto 2001). Surges in intensity of the downdrafts, resulting in additional surges in surface winds, were found to occur depending on variations in the specified cooling source (Hjelmfelt 1988; Proctor 1993; Anabor et al. 2011; Oreskovic et al. 2018), but unfortunately the causes of

Brought to you by Colorado State University Libraries | Unauthenticated | Downloaded 03/10/23 07:13 PM UTC

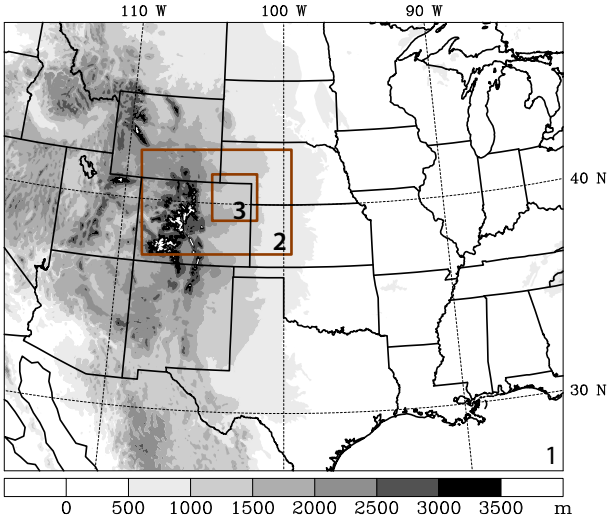

FIG. 3. Map of the WRF-ARW Model domains. The locations of domains 1, 2, and 3 are shown, and terrain is shaded.

these surges could not be explored without inclusions of microphysics in the simulations, at additional computational expense. Orf et al. (2012) found simulations with externally specified cooling sources were unable to fully capture microburst evolution compared to both observations and their idealized simulations using Cloud Model 1 (CM1) with full microphysics. Peak surface winds were found some distance behind the leading edge of the outflow and ring vortex, and the strongest winds (>30 m s^{-1}) were short in duration and highly variable. Only recently have mesoscale numerical models been used in an attempt to reproduce observed downburst events. van Dijke et al. (2011) was able to successfully simulate what they termed "microbursts," or swaths of peak winds with widths $O(5)$ km from a bow echo event over the Netherlands using the WRF Model, and Bolgiani et al. (2020) similarly reproduced a microburst event in northern Alabama with a 10-km footprint.

A common thread in all these simulations is their small spatial and temporal scale. While microbursts by definition have a diameter of less than 4 km and produce peak winds for no more than 5 min (Wakimoto 1985; Fujita 1990; Wakimoto 2001), it is surprising that none of the numerical simulations of severe winds induced by downdrafts described above produced damaging winds occurring on a larger scale. The severe winds associated with the 9 June 2020 macroburst were able to persist for at least 45 min and over 50 km, although still very localized in nature [cf. Figs. 10d and 11 of Childs et al. (2021)]. Such persistence suggests contribution by physical processes unlike those attributed to microburst generation. Numerical simulations of convectively generated severe winds *not* associated with either bow echoes or microbursts are rare, but previous studies do provide some hints of potential physical processes. For example, Proctor (1989) simulated a downburst occurring in an environment with a stable layer and found it excited gravity wave oscillations that spread ahead of the downburst head itself, widening the spatial impact of the system. The authors do not elaborate on wind speed perturbations associated with these waves, but do caution later in the text that such perturbations could easily be severe. Such long-lasting yet spatially localized severe winds also suggests comparison to downslope windstorms generated by a hydraulic jump forming on the lee side of a mountain partially blocking the flow (Clark and Peltier 1977, 1984; Sachsperger et al. 2017).

The unique nature of this event motivates a closer look to better identify and understand the small-scale features occurring within. Specifically, we turn to modeling to investigate the apparent wavelike features in the convection as well as understand the downburst signature in the context of potential elements such as gravity wave propagation, bores, and wave breaking. Two separate high-resolution model simulations are performed, one to simulate the observed event using the WRF Model, and one using simplified initial conditions in CM1. The proceeding section 2 presents an overview of the modeling frameworks. Results from the model simulations are shown in section 3, and a discussion of the mesoscale and misoscale processes is given in section 4, along with comparison to the observations. Section 5 concludes with a summary, application, and recommendations for future work.

2. Methods

Two numerical atmospheric models are used to simulate aspects of the 9 June 2020 downburst. Version 4.0.3 of the WRF-ARW Model (Powers et al. 2017) was used to conduct simulations of the observed event, both in a retrospective convection-permitting forecast mode and with a high-resolution nested configuration. The forecast configuration was equivalent to routine real-time forecasts performed at Colorado

TABLE 1. Summary of numerical model configurations for the simulations.

	WRF forecast	Nested WRF simulation	CM1 simulation
Horizontal grid spacing	4 km	267 m on innermost grid	125 m
Vertical grid	51 levels, stretched	80 levels, stretched	110 levels, stretched
Time step	25 s	1.33 s	0.5 s
Microphysics	Morrison	Thompson	Thompson
Planetary boundary layer	MYJ	MYJ	None; TKE scheme for turbulence
Radiation	RRTM	RRTM	None
Initial/lateral boundary conditions	0.5° GFS	0.5° GFS	0600 UTC WRF forecast sounding from Akron; warm bubble

Brought to you by Colorado State University Libraries | Unauthenticated | Downloaded 03/10/23 07:13 PM UTC

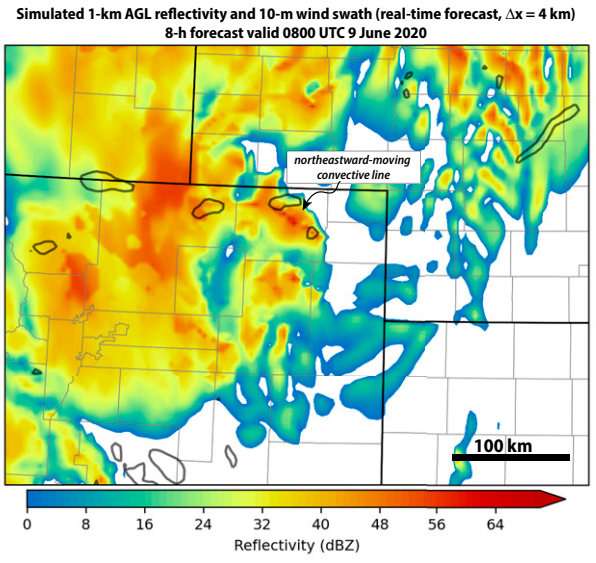

FIG. 4. Simulated radar reflectivity (dBZ, shaded) at 1 km AGL, and maximum 10-m wind speed since 0330 UTC (contour at 20 m s^{-1}) from the real-time forecast (Δx = 4 km) at 0800 UTC 9 Jun 2021.

State University, except rerun to generate more frequent history files. This configuration uses 4-km horizontal grid spacing over the outermost domain shown in Fig. 3, with initial and lateral boundary conditions from 0.5° latitude–longitude resolution GFS forecasts updated every 3 h. The simulation shown in this study was initialized at 0000 UTC 9 June 2020, approximately 6 h prior to the observed downburst. Although this provides a relatively short model "spinup" time from coarse initial conditions, forecasts initialized at earlier times did not produce reasonable representations of the observed convection, whereas this initialization time did so without any obvious spurious artifacts. The physical parameterizations (summarized in Table 1) included the Mellor–Yamada–Janjić (MYJ; Mellor and Yamada 1982; Janjić 2002) planetary boundary layer (PBL) parameterization, the Morrison et al. (2009) two-moment cloud microphysics parameterization, the Noah (Chen and Dudhia 2001) land surface model, and the Rapid Radiative Transfer Model for GCMs (Iacono et al. 2008).

As shown in Childs et al. (2021) and in section 3a, this forecast produced a line of storms in northeast Colorado that resembled the structure of the observed convective line, but it was displaced in space and time and did not produce wind speeds nearly as strong as those observed. To determine whether insufficient model resolution was one of the reasons for this underprediction, we conducted additional simulations with higher-resolution nested grids. We experimented with different model configurations, and found that higher-resolution simulations using the Thompson et al. (2008) microphysics parameterization produced convective systems that corresponded better with observations. (In contrast, at 4-km grid spacing, the Morrison et al. and Thompson et al. schemes produced very similar results to each other.) Simulations using a

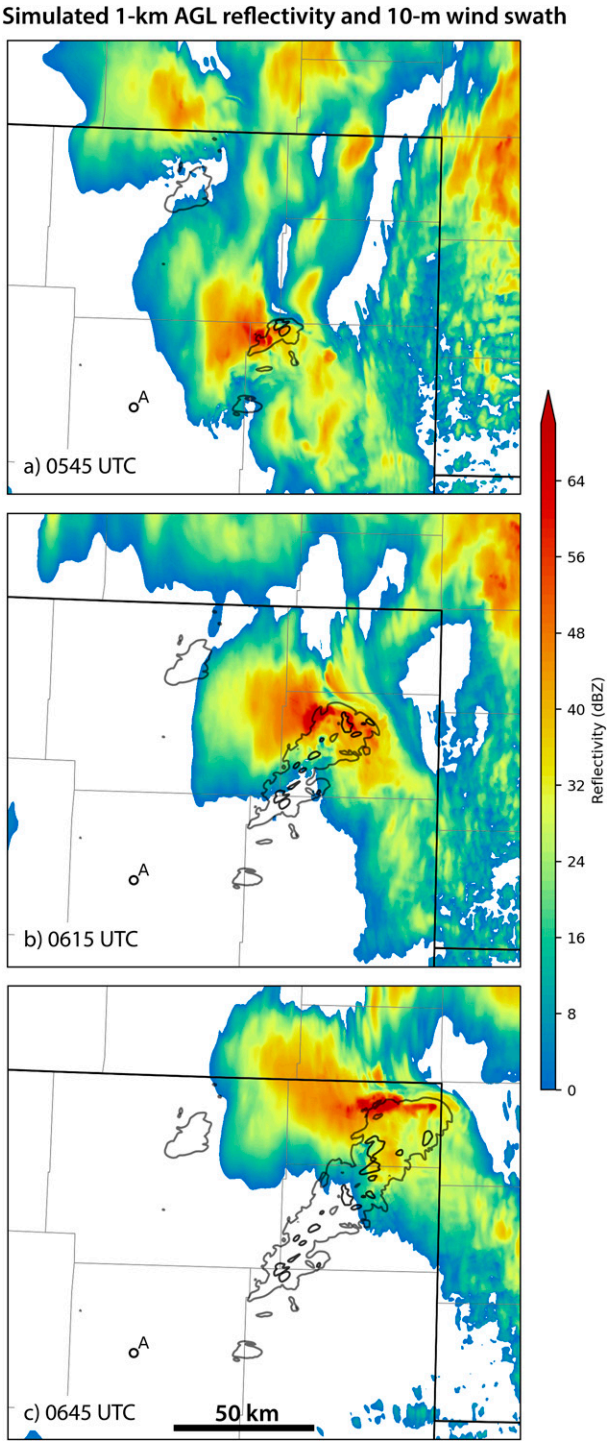

FIG. 5. Simulated radar reflectivity (dBZ, shaded) at 1 km AGL, and maximum 10-m wind speed since 0330 UTC (contours at 30 and 40 m s^{-1}) from WRF simulation domain 3 (Δx = 267 m) at (a) 0545, (b) 0615, and (c) 0645 UTC 9 Jun 2020. The location of Akron is indicated in each panel.

Brought to you by Colorado State University Libraries | Unauthenticated | Downloaded 03/10/23 07:13 PM UTC

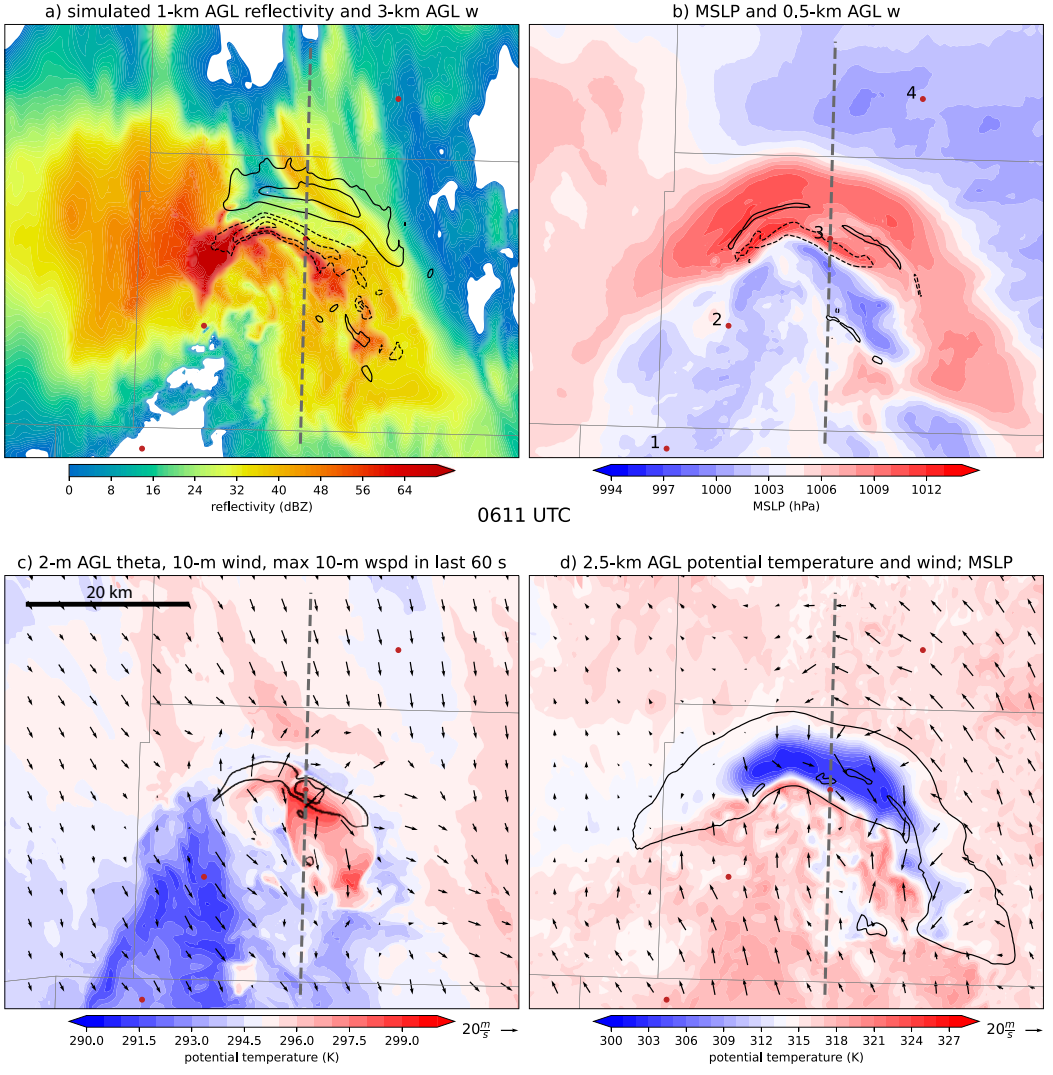

FIG. 6. Output from domain 3 of the WRF simulation at 0611 UTC 9 Jun 2020. (a) Simulated radar reflectivity (dBZ, shaded) at 1 km AGL and vertical velocity at 3 km AGL (contours every 10 m s^{-1}, zero contour omitted, negative contours dashed). (b) Mean sea level pressure (hPa, shaded) and vertical velocity at 500 m AGL (contours every 10 m s^{-1}, zero contour omitted, negative contours dashed). (c) Potential temperature at 2 m AGL (K, shaded), maximum 10-m wind speed in the previous minute (contours at 30 and 40 m s^{-1}), and 10-m wind vectors. (d) Potential temperature at 2.5 km AGL (K, shaded), mean sea level pressure (contoured at 1007 and 1012 hPa), and 2.5-km wind vectors. Locations of time series points are indicated with brown dots; numbers of these points are shown in (b). The gray dashed line shows the location of vertical sections shown in subsequent figures.

single nest at 800-m grid spacing (not shown) produced a broad swath of severe winds in northeastern Colorado, so we proceeded to include a third nest at 267-m horizontal grid spacing (Fig. 3). The third grid was added at 3 h 30 min into the simulation to conserve computational expense. Output from this grid will be the primary focus of section 3b.

Then, to focus on specific convective processes, we also conducted simulations using Cloud Model 1 (Bryan and Fritsch 2002). These simulations used a horizontally homogeneous base state that was obtained from a profile at 0600 UTC near Akron, Colorado, in the 4-km WRF simulation (to be shown and discussed in more detail in section 3). The horizontal grid was 1200 × 1200 grid points with 125-m horizontal spacing. The vertical grid used 110 vertical levels on a stretched grid with spacing of approximately 35 m near the surface increasing to 250 m aloft. Convection was initiated with a single warm bubble centered at 1.4 km AGL with a radius of 10 km and a maximum potential temperature perturbation of 2 K. Sensitivity tests that varied the initial height of the bubble produced qualitatively similar results. The model domain was translated at $u = 5$ m s^{-1} and $v = 10$ m s^{-1} to keep the convection near the center of the domain. The simulation was integrated

Brought to you by Colorado State University Libraries | Unauthenticated | Downloaded 03/10/23 07:13 PM UTC

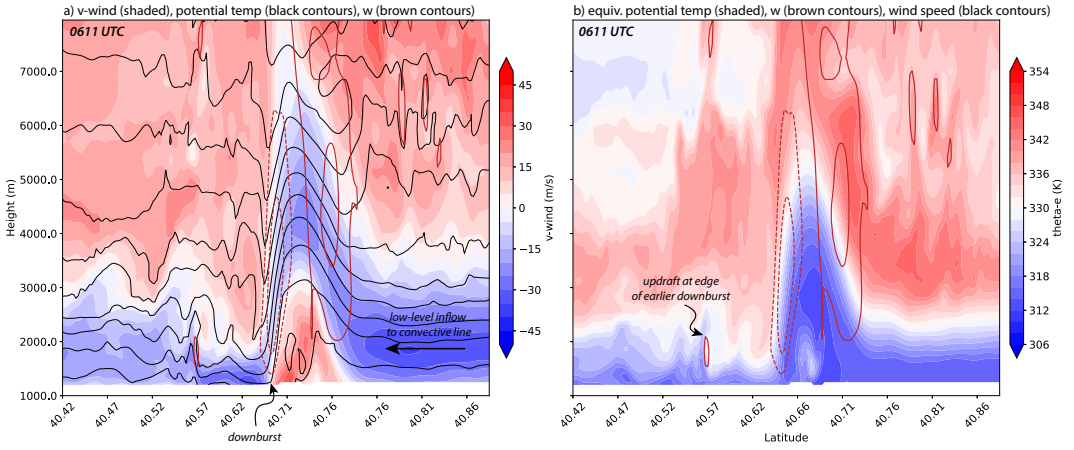

FIG. 7. Vertical section through the line shown in Fig. 6 from domain 3 of the WRF simulation at 0611 UTC 9 Jun 2020. (a) Meridional wind (shaded, m s^{-1}), potential temperature (black contours every 4 K), and vertical velocity (brown contours every 10 m s^{-1}, zero contour omitted, negative contours dashed). (b) Equivalent potential temperature (K, shaded), vertical velocity (brown contours every 10 m s^{-1}, zero contour omitted, negative contours dashed), and wind speed (black contours at 30, 40, and 50 m s^{-1}).

for 2.25 h. As with the WRF simulation, the Thompson et al. (2008) microphysical parameterization was used. No radiation or Coriolis accelerations were applied. The upper and lower boundaries were free slip, and open-radiative boundary conditions (Durran and Klemp 1983) were used to ensure that outward mass flux does not exceed inward. The properties of 288 000 air parcels initialized at $t = 55$ min in the lowest 4 km were calculated at each model time step. Other details of the model configuration, and comparisons with the WRF simulations, are given in Table 1.

3. WRF simulations

a. *Real-time forecast, $\Delta x = 4$ km*

In the real-time WRF forecast at 4-km horizontal grid spacing, convection initiated in eastern Colorado and across Nebraska to the north of the cold front, with storm motions toward the northeast, similar to observations [Fig. 4; see also Childs et al. (2021)]. As with the observed system, most of the convection organized into short northwest–southeast-oriented lines, but a couple convective bands became oriented approximately west–east, and produced strong winds as they moved toward the north-northeast in eastern Colorado. One of these convective lines is highlighted in Fig. 4. Unlike the observations of extremely strong wind speeds, however, the real-time forecast only produced maximum 10-m winds of 20–25 m s^{-1} in northeast Colorado. The underprediction of wind speeds was consistent with other convection-allowing forecast models (Childs et al. 2021).

Nonetheless, this forecast model output suggests wavelike convective structures that resembled the observed system (not shown), and motivated further experiments to simulate this event at higher resolution, to determine whether a more realistic simulation of the 9 June 2020 downburst could be obtained.

b. *Nested simulation, $\Delta x = 267$ m*

With a nested grid at 267-m horizontal grid spacing and using the Thompson microphysics parameterization (section 2), the evolution of the convection in northeast Colorado was similar to the coarser-resolution run, but produced a swath of very intense surface winds (Fig. 5). The structure of the downburst-producing convective line closely resembled the observed system, with a small bowing segment on its eastern end, although the simulated line was displaced approximately 60 km to the northeast of the observed system (cf. Figs. 5 and 1). A swath of winds exceeding 30 m s^{-1} was simulated with the simulated convective line, and within that swath were numerous areas exceeding 45 m s^{-1} that were associated with localized downbursts (Fig. 5). This compares closely with observed wind gusts, which exceeded 30 m s^{-1} at multiple stations and topped 50 m s^{-1} in Akron (Fig. 2).

The structure of the severe-wind-producing convective line was characterized by an arc-shaped region of high pressure at the surface, with mean sea level pressure over 10 hPa higher than the surroundings in the area between the midlevel updraft and downdraft (Figs. 6a,b). Ahead and behind this band of high pressure were areas of relatively low pressure. There was relatively cool air at the surface well behind the convective line, but nearer to the line were surface warm anomalies in the vicinity of low-level descent and very strong surface winds (Figs. 6b,c). Above the surface, however, was a band of very low potential temperature with respect to the ambient environment; potential temperature deficits in this band at 2.5 km AGL were 10–15 K (Fig. 6d). Together, these features—no surface cold pool, a low–high–low pressure pattern, and an elevated region of cold air—point to this convective line being characterized as a gravity wave, as opposed to a cold-pool-driven system.

The wave structure of this system is further illustrated in vertical sections through the convective line (Fig. 7). Between

Brought to you by Colorado State University Libraries | Unauthenticated | Downloaded 03/10/23 07:13 PM UTC

the convective updraft and downdraft, isentropes have been raised in the layer from approximately 2–6 km MSL (Fig. 7a). This is a reflection of the negative potential temperature perturbation seen at 2.5 km AGL in Fig. 6d. Furthermore, the potential temperature perturbation being out of phase with the vertical motion is expected of a gravity wave (e.g., Markowski and Richardson 2010). The low-level flow is from the north, and thus as air approaches from the right (in the plane of this vertical section), it rises along these raised isentropes and eventually ascends into the convective line. Just to the south of the upward motion is the descending branch of the wave, with downdrafts of similar magnitude to the updrafts (Figs. 7a,b). Isentropes (and pseudoisentropes) in this descending branch have become tightly packed and oriented nearly vertically. Some of the strong downdrafts reach the surface, resulting in a downburst with winds exceeding 40 m s^{-1} (Fig. 7b). These near-surface wind speeds are stronger than those found in the lowest several kilometers of the environment, suggesting that they are not being produced by simply the downward transport of momentum. Animations (included in the online supplemental material) reveal this behavior repeating several times as the convective line moved to the northeast; the upward motion that occurred along the edge of an earlier downburst is also apparent in Fig. 7b.

Surface time series from the simulation (output every model time step) show many similarities to the observations discussed in Childs et al. (2021) and shown in Fig. 2, but also some noteworthy differences. At each of the four points shown in Fig. 8, which were selected to highlight severe winds in different parts of the simulated line's progression, the maximum 10-m wind speeds exceeded 35 m s^{-1}. They also showed a sharp decrease in wind speed shortly after the initial peak, followed by a secondary maximum in wind speed, consistent with downbursts and with observations. All of these time series showed large pressure increases of 10–15 hPa as the line and associated gravity wave passed, followed by rapid pressure drops. With the exception of point 1, where the convective line passed very early in its life (Fig. 8a), the temperature rose sharply, coincident with or shortly after the peak winds, followed by a decrease to temperatures lower than the pre-storm environment. These features are all very consistent with the high-resolution surface observations of the line's passage [cf. Figs. 2 and 8, and also Fig. 13 of Childs et al. (2021) which shows a longer time series of pressure].

In contrast, some features of the simulated surface observations do not align with the observed features. For example, in the simulation, the pressure dropped before rising sharply, and then fell back to near the values from the pre-storm environment. On the other hand, the observations did not show a substantial pressure drop prior to the sharp increase but was rather nearly constant, and then following the uptick decreased to several hPa below the values from the pre-storm environment. Furthermore, the time series at points 1–3 showed stronger cooling in the minutes immediately prior to the peak winds than observed. The time series at point 4—the northeasternmost of the points analyzed here—appears to compare most closely to the observed time series (cf. Figs. 2 and 8d) Considering that the highest-resolution observations were only available at a single location, it is not clear whether the differences represent variations within the system that were not sampled, inconsistencies between the simulated and observed system, or both. Nonetheless, the overall agreement between the model output and observations provides some confidence that the simulation is adequately representing many of the important processes in the observed event.

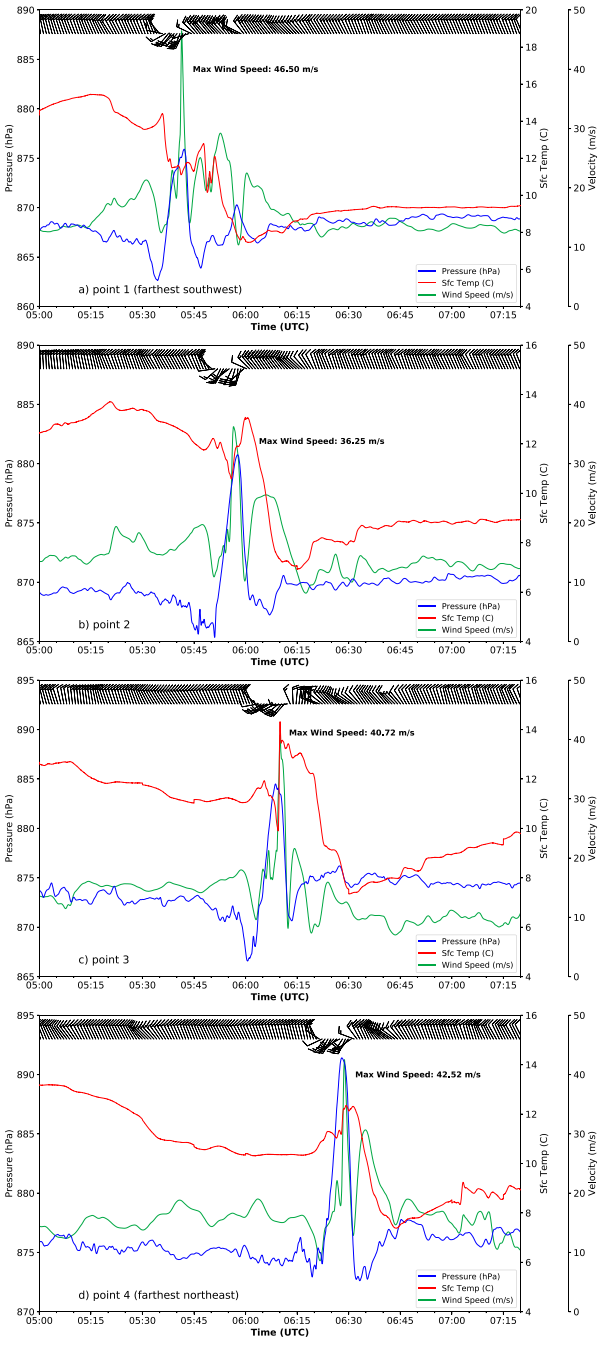

FIG. 8. As in Fig. 2, but for model output from domain 3 of the WRF simulation at the four points shown in Fig. 6b. Model output is shown at each time step (every 1.33 s).

Brought to you by Colorado State University Libraries | Unauthenticated | Downloaded 03/10/23 07:13 PM UTC

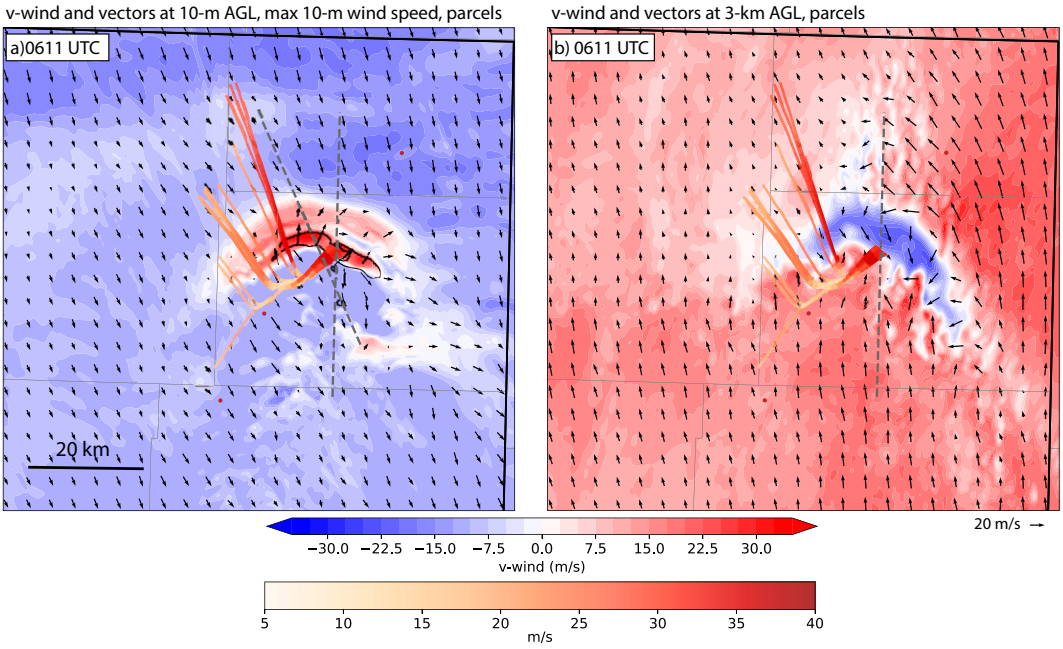

FIG. 9. (a) Meridional wind (shaded) and wind vectors (m s^{-1}) at 10 m AGL, maximum 10-m wind speed in the previous minute (contours at 30 and 40 m s^{-1}), and selected backward parcel trajectories (shaded by wind speed in m s^{-1}) ending at 0611 UTC 9 Jun 2020 from domain 3 of the WRF simulation. (b) As in (a), but meridional wind and vectors are at 3 km AGL.

To further diagnose the processes associated with the downbursts in the model simulation, a series of backward parcel trajectories were calculated using the Read-Interpolate-Plot (RIP; Stoelinga et al. 2018) program. Namely, a grid of locations was defined surrounding the locations of the surface time series shown in Fig. 8 below 500 m AGL. Parcel trajectories were integrated backward from these points from the approximate time of the peak observed near-surface wind speed, with the purpose of identifying the properties of the air that ended up in the downbursts. Trajectories were integrated backward for 40 min. The focus here is on the backward trajectories initialized from point 3 at 0611 UTC; trajectories initialized from the other points showed generally similar characteristics.

This analysis reveals that the downburst air parcels (defined here as those with wind speed $\geq$ 34 m s^{-1} between 0609 and 0611 UTC) largely originated in the lowest 1 km AGL to the north-northwest of the convective line, within the postfrontal flow (Figs. 9a and 10). Two clusters of parcels are apparent, with one set at approximately 500 m AGL, and another closer to the surface (Fig. 10a); the wind speeds of the respective parcels illustrate the strong low-level vertical shear. As this air approaches the convective line, it ascends along the leading edge of the low-level gravity wave. These parcels then reach a layer of weak *southerly* winds (Fig. 9b). They rapidly decelerate and reverse direction. Concurrently, the gravity wave is amplifying and steepening (Figs. 10a,b). Then, the parcels enter the downward branch of the gravity wave, and descend rapidly to the surface, where they accelerate again and become part of the downburst with intense near-surface winds (Figs. 9 and 10b,c).

This sequence of processes represents a different mechanism for an intense downburst than the conventional mechanisms associated with hydrometeor loading or strong subcloud evaporative cooling. Instead, the processes are more akin to the wave ducting and breaking beneath a critical level that occurs in mesoscale gravity waves and severe downslope windstorms (e.g., Clark and Peltier 1977, 1984; Peltier and Clark 1979; Durran 1990; Ruppert et al. 2022). As discussed above and by Childs et al. (2021), the environment ahead of the convective line was characterized by a strong temperature inversion above the cool postfrontal air mass, with very strong low-level vertical wind shear (Figs. 11a,b). This thermodynamic profile resembles those previously associated with mesoscale gravity waves (Ruppert et al. 2022, their Fig. 1b). The inversion strength was maximized at approximately 1.3 km AGL (Fig. 12a). For a gravity wave moving to the north-northeast, the component of the wind perpendicular to the wave motion was very strong with respect to the wave motion at low levels (exceeding 40 m s^{-1}; Fig. 12b), and then decreased to zero just above 4 km AGL. This represents a critical level, beneath which vertically propagating waves would be trapped and may break. These parameters are combined in the Scorer parameter, which is often used in analyzing mountain wave behavior (e.g., Markowski and Richardson 2010) but increasingly also used to understand convectively generated gravity waves (e.g., Haghi et al. 2017, 2019). The Scorer parameter is defined as

Brought to you by Colorado State University Libraries | Unauthenticated | Downloaded 03/10/23 07:13 PM UTC

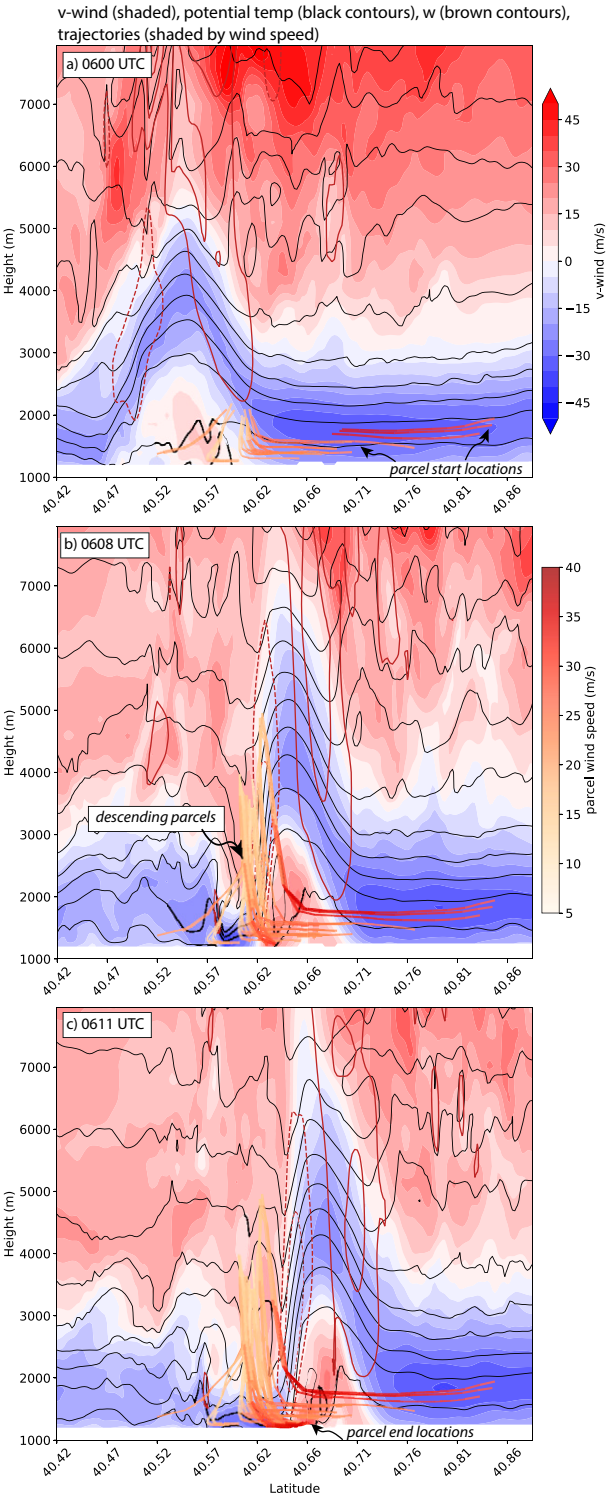

FIG. 10. As in Fig. 7a, but with selected backward parcel trajectories, projected in the y–z plane (shaded by wind speed in m s^{-1}) ending at (a) 0600, (b) 0608, and (c) 0611 UTC 9 Jun.

$$l_s^2 = \frac{N^2}{(U-c)^2} - \frac{U_{zz}}{U-c}, \tag{1}$$

where N is the Brunt–Väisälä frequency, $U(z)$ the horizontal wind speed with respect to height in the direction of the wave, and c is the wave phase speed (calculated to be 19 m s^{-1} at 32.5° to the northeast). The Scorer parameter spiked to very large values at just above 4 km AGL (Fig. 12c), the critical layer for north-northeastward-moving waves. (With $U - c$ approaching zero, the first term of the Scorer parameter becomes very large. The second term, associated with the curvature of the wind profile, was about an order of magnitude smaller at this level.) The Scorer parameter was also relatively large where N^2 peaked at around 1.3 km, though much smaller than the values in the spike near 4 km (shown in Fig. 12c, though difficult to see).

Wave trapping can be facilitated by layers where the Scorer parameter decreases sharply with height, and wave breaking may occur beneath critical levels, both of which are present in this environment. Thus, we hypothesize that a gravity wave produced by the convective line amplified and broke between the low-level inversion and the critical level, leading to intense downdrafts at the surface that were stronger than any winds in the layers above the surface. These processes will be explored further in the following discussion of the CM1 simulation as well as section 4.

4. CM1 simulation

The WRF simulation faithfully represented many aspects of the observed event, but further questions remain, such as the respective roles of storm-generated processes and larger-scale forcing mechanisms. The WRF simulation was also run at a grid spacing where the need for a planetary boundary layer parameterization is unclear, and parcel trajectories must be run using postprocessed output rather than in line with the model integration. For these reasons, a simulation using horizontally homogeneous initial conditions in CM1 was also conducted to complement the WRF results. The configuration for this simulation was discussed in section 2, and the initial condition was the sounding shown in Fig. 11, which came from the real-time WRF forecast at Akron.

After the initiation of convection with a single warm bubble, a convective line developed that in many ways resembled the observed and WRF-simulated systems. The line moved toward the north-northeast, and produced a broad swath of severe winds at the surface (Fig. 13). The strongest gusts in the CM1 simulation exceeded 70 m s^{-1}, with widespread winds exceeding 50 m s^{-1}. These wind speeds are much greater than those observed, which is likely a result of the free-slip lower boundary condition used in the simulation (i.e., there was no friction to slow the near-surface winds). Nonetheless, it is notable that convection initiated with a single warm bubble in the 9 June 2020 environment organized into a severe-wind-producing convective line with no other external forcing, echoing the findings of Hitchcock and Schumacher (2020)

Brought to you by Colorado State University Libraries | Unauthenticated | Downloaded 03/10/23 07:13 PM UTC

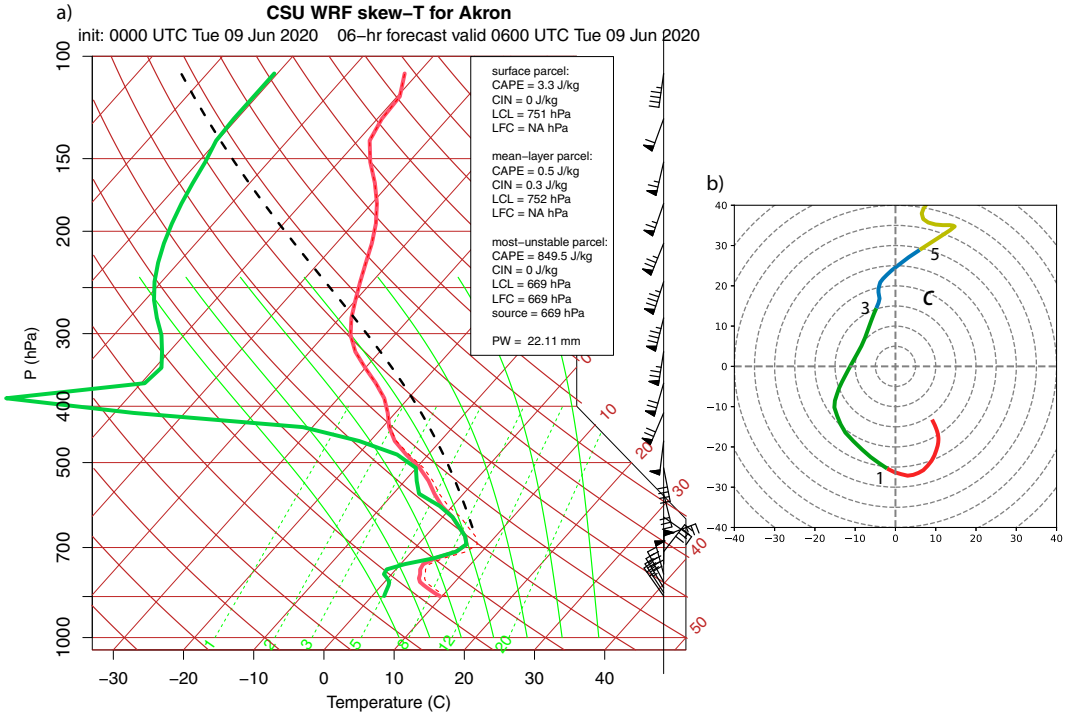

FIG. 11. Vertical profiles from the real-time WRF forecast at 0600 UTC 9 Jun 2020 at Akron, shown in Fig. 1. (a) Skew T–log$p$ diagram. The black dashed line shows the temperature of the most unstable parcel. Half barbs indicate winds of 5 kt; full barbs indicate winds of 10 kt, and pennants indicate winds of 25 kt. (b) Wind hodograph (m s^{-1}) for the lowest 8 km AGL, with the color changing at heights of 1, 3, and 5 km AGL. The wave motion of 19 m s^{-1} toward 32.5° east of north, estimated from the nested WRF simulation, is shown by the letter C on the hodograph.

and Parker (2021) in nocturnal environments with strong stable layers.

The reflectivity, pressure, wind, and potential temperature patterns associated with the simulated convective line all largely resembled those of the WRF simulation (Figs. 14 and 15). Specifically, a gravity wave structure with low-level ascent ahead of the highest reflectivity, a large increase in surface pressure, and an elevated band of strong cooling were all simulated. Unlike the WRF simulation, however, there was little near-surface cooling behind the convective line, suggesting that cold-pool processes were not crucial to the overall evolution of the system (cf. Figs. 15c and 6c).

Figures 14 and 15 also illustrate the transition from the strongest surface winds having a linear orientation, to the development of strong downbursts, which occurred several times during the simulation. At t = 68 min, the convective line was approaching the point shown in Fig. 14, with a line of surface winds exceeding 50 m s^{-1} (Fig. 14c). Ten minutes later, that location had winds greater than 70 m s^{-1}, as a macroburst occurred between the ascending and descending branches of the gravity wave (Fig. 15c).

Vertical sections through the system show the evolution of the gravity wave over this 10-min period, as the wave (shown by the elevated cool perturbation in Fig. 16, representing upward displacement of isentropes) amplified, and the descending branch steepened. The wave evolved between the heights of the initial low-level inversion at about 1.2 km AGL and the critical level at about 4.2 km AGL, with the wave likely trapped between these two layers. Downdrafts intensified markedly over this 10-min period, bringing potentially warm air downward, and some reached the surface, resulting in very strong winds beneath the wave. Notably, nowhere in the layer between just above the surface and approximately 5 km AGL had wind speeds of 40 m s^{-1} or greater; these intense winds only occurred in a shallow layer very near the surface. Figure 17 gives a different view of these features at t =78 min, showing tightly packed, overturned isentropes at the descending branch of the wave, and a swath of intense winds, with southerly winds beneath the wave and multiple smaller downbursts behind it, as well as some strong low-level updrafts on the north edge of the downbursts.

Air parcel trajectories, which in CM1 run inline (rather than being calculated later from the model output), show similar characteristics to those calculated from the WRF output. For the purpose of illustration, two parcels were selected, both of which obtain near-surface wind speeds of over 60 m s^{-1} (Fig. 18; animation included in the online supplement). One of these parcels approaches the convective line within a layer of strong winds from the north at approximately 1 km AGL. As

Brought to you by Colorado State University Libraries | Unauthenticated | Downloaded 03/10/23 07:13 PM UTC

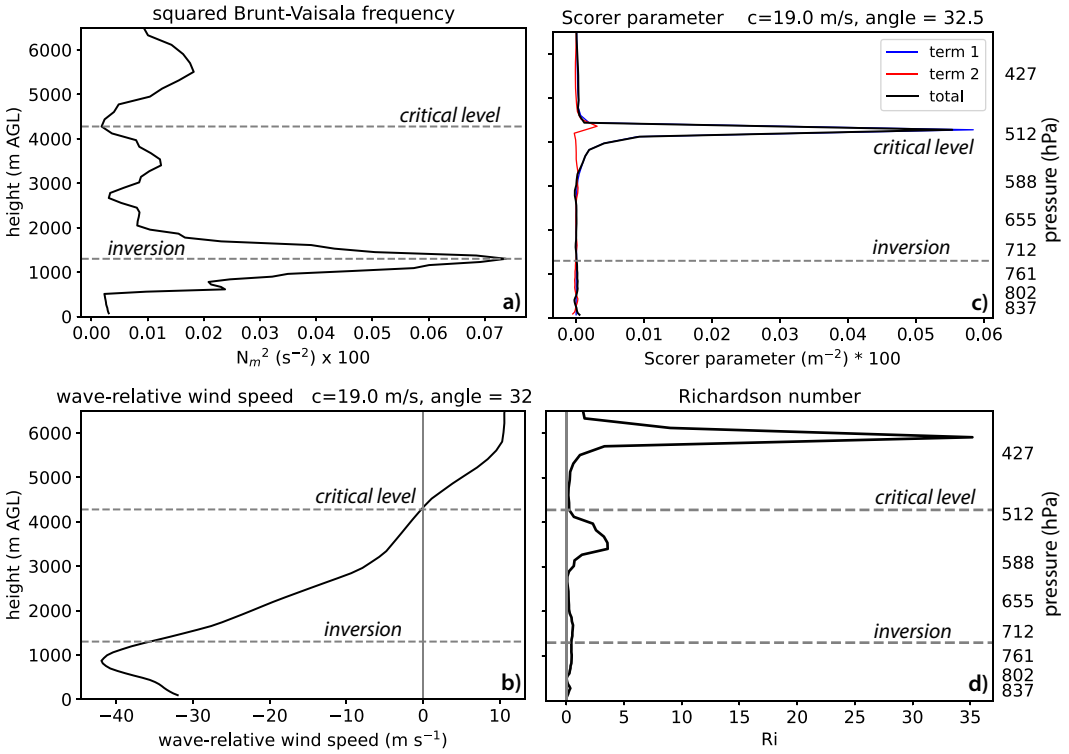

FIG. 12. Vertical profiles of the sounding shown in Fig. 11, showing (a) squared moist Brunt–Väisälä frequency multiplied by 100 (s^{-2}); (b) $U - c$, the wind component perpendicular to the wave and relative to the wave motion; (c) the Scorer parameter multiplied by 100 (m^{-2}), assuming a wave motion of 19 m s^{-1} toward 32.5° east of north, which was estimated from the nested WRF simulation; and (d) Richardson number. Heights of the peak of the stable layer and the critical level are shown with dashed lines and annotated.

with the WRF-calculated parcels, it ascends rapidly in the upward branch of the wave and decelerates. This parcel then descends, but prior to reaching the surface, ascends again briefly, before sinking and reaching the surface with >60 m s^{-1} winds. The second parcel takes a somewhat different path, originating near the surface to the west of the convective line, and then looping upward and downward behind the line, before descending, accelerating, and moving to the east. Other parcels that were part of intense downbursts (omitted for clarity) behaved similarly to the two shown here. In total, the vast majority of the parcels that attain intense wind speeds near the surface originated below 1.5 km AGL, rather than farther aloft (Fig. 19). The results of this trajectory analysis—calculated in an entirely different manner than the WRF-based trajectories—provide further evidence that the strongest winds were associated with air that originated at low levels, moved through the convectively generated gravity wave, and rapidly descended, with stronger wind speeds at the surface than anywhere in the layer immediately above.

5. Discussion

To summarize the previous sections, three specific features of the macroburst simulations suggest wave activity generating the severe surface winds as opposed to being cold-pool-driven:

- Simulations both with (WRF) and without (CM1) surface cooling exhibited the severe winds,

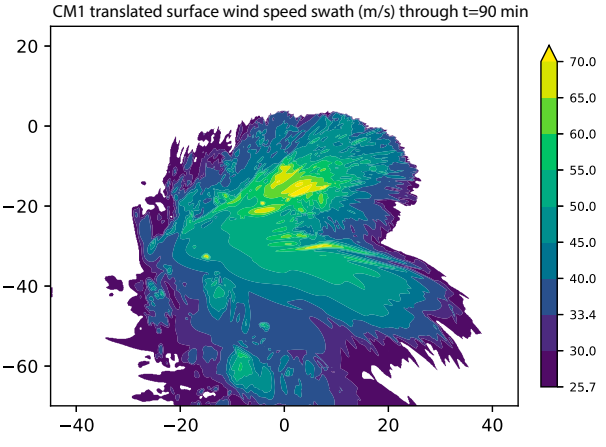

FIG. 13. Maximum wind speed at the lowest model level (m s^{-1}), translated to account for the moving model domain, through t = 90 min of the CM1 simulation.

Brought to you by Colorado State University Libraries | Unauthenticated | Downloaded 03/10/23 07:13 PM UTC

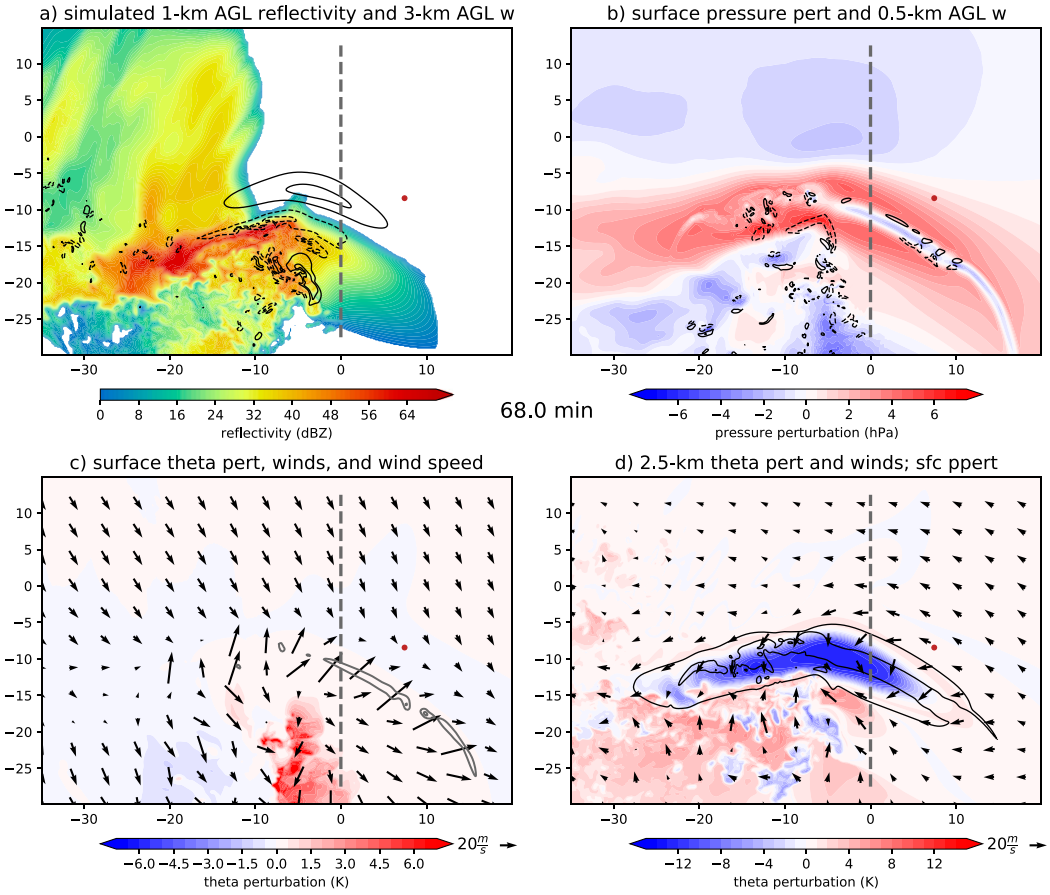

FIG. 14. Output from the CM1 simulation at $t = 68$ min. (a) Simulated radar reflectivity (dBZ, shaded) at 1 km AGL and vertical velocity at 3 km AGL (contours every 10 m s^{-1}, zero contour omitted, negative contours dashed). (b) Surface pressure perturbation (hPa, shaded) and vertical velocity at 500 m AGL (contours every 10 m s^{-1}, zero contour omitted, negative contours dashed). (c) Potential temperature perturbation (K, shaded), wind speed (gray contours at 50, 60, and 70 m s^{-1}), and wind vectors, all on the lowest model level. (d) Potential temperature perturbation at 2.5 km AGL (K, shaded), surface pressure perturbation (contoured at 3 and 6 hPa), and 2.5-km wind vectors. The gray dashed lines show the location of vertical sections shown in subsequent figures.

- Severe winds occurred over a small spatial but long temporal period, and
- The vertical motion field was out of phase with the potential temperature perturbations.

Previous microburst modeling studies have emphasized the importance of low-level cooling on generating the subsequent severe winds (Proctor 1988, 1989; Hjelmfelt 1988). Microphysical causes, both through latent cooling and precipitation loading, were the sole progenitors of the downbursts, with the resulting pressure gradient converting the motion from vertical to horizontal upon parcels reaching the surface (Orf et al. 2012). However, such a translation is not perfect, resulting in a reduction in wind speeds the farther the gust front travels from the initial downdraft. In contrast, in these simulations severe surface winds were produced for over an hour. This production occurred independent of a surface cold pool in the CM1 simulation, and without strong winds aloft to translate momentum to the surface. Further, the pressure gradient at the location of the strong winds pointed *opposite* the wind direction. For example, Fig. 6c shows the strongest 10-m wind speeds occurring at point 3, with the winds themselves blowing to the northeast (Fig. 8c). The pressure gradient at point 3, however, is oriented to the southwest as the peak portion of the meso-high had already passed the station. Similarly, in each time series (Figs. 2 and 8) the pressure rose significantly before the wind speeds peaked. Conversely, peak winds are expected to occur ahead of the pressure peak for more traditional gust front or cold-pool-driven features [e.g., Fig. 29 of Wakimoto (1982)].

After accepting the existence of wave activity, it is next reasonable to seek a framework from the literature in which to place the feature. Wavelike features produced by convection can be considered using a number of frameworks, including hydraulic theory (e.g., Rottman and Simpson 1989; Haghi et al. 2017) and linear wave theory (e.g., Knupp 2006; Haghi et al. 2017; Haghi and Durran 2021). A few complications suggest neither option is acceptable in this case. Hydraulic

Brought to you by Colorado State University Libraries | Unauthenticated | Downloaded 03/10/23 07:13 PM UTC

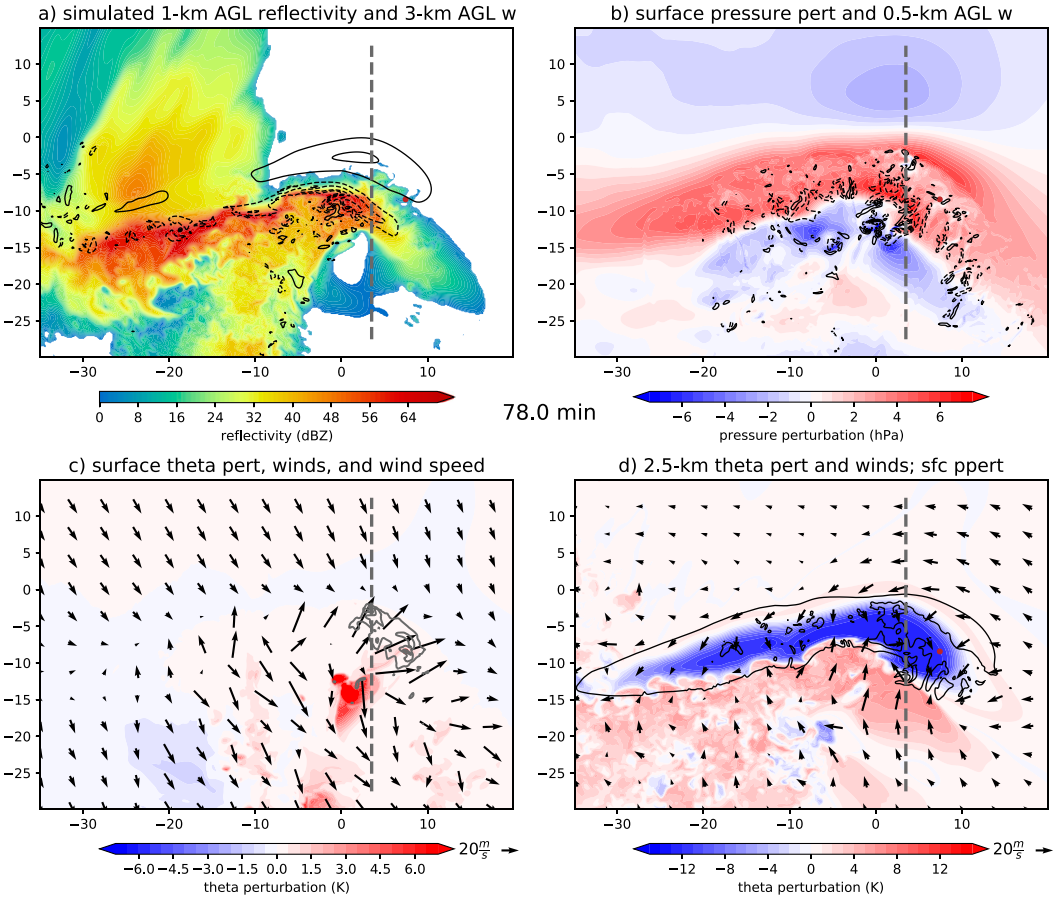

FIG. 15. As in Fig. 14, but at $t = 78$ min.

theory, while ideal for understanding flow over an obstacle such as a mountain or cold pool, is not designed to incorporate vertical restoring forces resulting from variations in shear and/or stability over the flow depth in question (Haghi et al. 2017; Haghi and Durran 2021). The highly varying vertical wind and stability profiles over the surface to 5 km layer (e.g., Figs. 11 and 12) will both allow and impede vertical propagation of any generated wave energy, limiting the usefulness of the hydraulic/shallow water theory framework in this case.

Linear wave theory suggests wave trapping could occur if the square of the Scorer parameter [Eq. (1)] decreases sufficiently with height. Recent work by Haghi and Durran (2021) has noted that this equation should be solved as an eigenvalue–eigenfunction problem to truly identify occurrence of wave trapping. In one particular instance, however, such an approach is not necessary: if the horizontal wind speed at a given layer exactly opposed the wave phase speed, the second term's denominator is 0. This critical layer does not allow wave energy to propagate vertically through it. In fact, nonlinear waves encountering the layer were found by Clark and Peltier (1977) to be reflected almost entirely, losing little amplitude. Such a critical layer is evident in this case just above 4 km (Fig. 12). If the Richardson number is less than 0.25 at that critical level, amplification of the wave can occur (Clark and Peltier 1977; Peltier and Clark 1979). At the critical level in this case, the Richardson number was indeed less than 0.25 from the critical level up to 4774 m AGL (Fig. 12d).

If amplification of wave energy continues, nonlinear effects further increase, and local overturning of the potential temperature contours and wave breaking can occur (Lilly 1978; Christie 1989). Such conditions have been found in association with multiple severe downslope windstorm events (Lilly 1978; Clark and Peltier 1977; Peltier and Clark 1979). Comparison of the potential temperature field at the time of the severe winds in Fig. 10b from the WRF run, or Fig. 17 from the CM1 run, with the potential temperature and wind fields analyzed by Lilly [1978, his Figs. 7 and 9; see also adapted Figs. 12.9 and 12.10 of Markowski and Richardson (2010)] during the 11 January 1972 severe downslope windstorm in Boulder, Colorado shows strong similarities, including the overturning potential temperature contours the air parcels travel through before swift acceleration to the surface, and the near-zero wind at midlevels above the downslope winds. The analogy between the two processes does fail in one respect. In the macroburst, upon nearing the surface the winds are redirected back toward the prestorm region of inflow, or toward the north. In a downslope windstorm, winds continue

Brought to you by Colorado State University Libraries | Unauthenticated | Downloaded 03/10/23 07:13 PM UTC

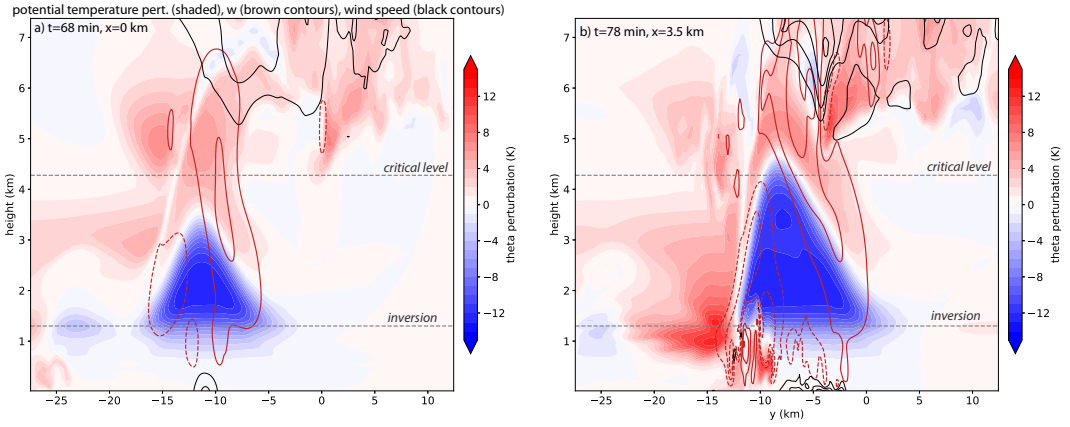

FIG. 16. Vertical section through the lines shown in Figs. 14 and 15 of potential temperature perturbation (shaded, K), vertical velocity (brown contours every 10 m s^{-1}, zero contour omitted, negative contours dashed), and wind speed (black contours at 40, 50, 60, and 70 m s^{-1}) from the CM1 simulation at (a) $t = 68$ and (b) $t = 78$ min. The heights of the initial inversion and critical level (as in Fig. 12) are shown with dashed lines.

in the same direction during and after acceleration toward the surface. It is clear, however, given the overturning isentropes, that large nonlinear wave effects and wave breaking below a critical layer were what produced the extreme, long-lived winds in the 9 June 2020 macroburst event.

While the existence of the critical level explains how the wave amplification and eventual breaking could occur, it does not explain how a gravity wave could be generated initially. Review of the CM1 perturbation potential temperature field showed that wave processes developed very early in the simulation at 16 min (see animation in supplementary information). At this time a cold pool had not yet developed, nor have significant latent cooling processes, making generation of wave processes by a cold pool impacting the low-level stable layer unlikely. However, latent heating processes were occurring at that time in association with a developing updraft, and were concentrated in the 1–4 km layer. A gravity wave generated by the onset of this latent heating would have been at the appropriate height to be trapped between the critical layer and the stable inversion below.

6. Conclusions

In this study, numerical simulations of the destructive 9 June 2020 macroburst were conducted in both case-study mode with the WRF Model and with simplified initial conditions in CM1. Both simulations revealed convective structures that compared favorably with the high-resolution observations presented by Childs et al. (2021), including a swath of intense surface winds and rapid fluctuations in temperature and pressure. Furthermore, the simulations clearly showed that the convection was associated with development and amplification of a gravity wave that eventually broke, resulting in repeated downbursts at the surface. Downburst wind speeds at the surface

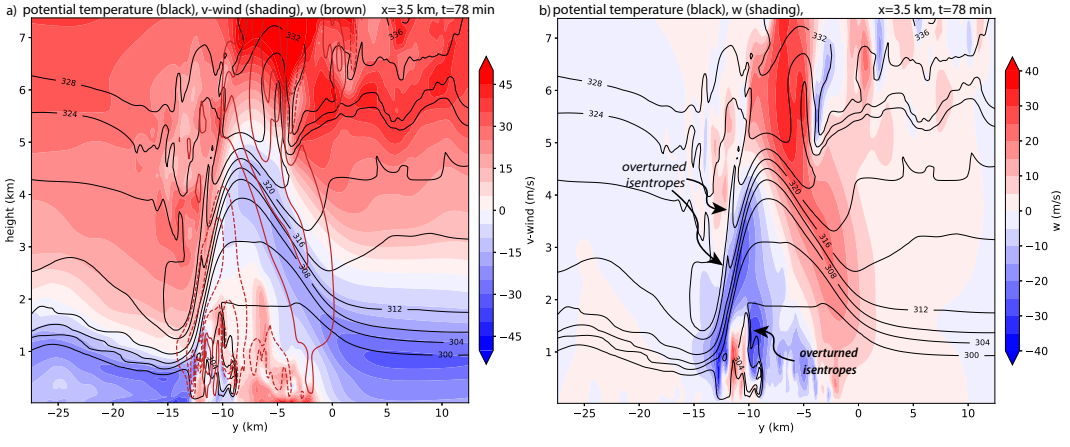

FIG. 17. (a) Vertical section through the line shown in Fig. 15 of meridional wind (shaded, m s^{-1}), potential temperature (black contours every 4 K), and vertical velocity (brown contours every 10 m s^{-1}, zero contour omitted, negative contours dashed) from the CM1 simulation at $t = 78$ min. (b) As in (a), but for vertical velocity (shaded, m s^{-1}).

Brought to you by Colorado State University Libraries | Unauthenticated | Downloaded 03/10/23 07:13 PM UTC

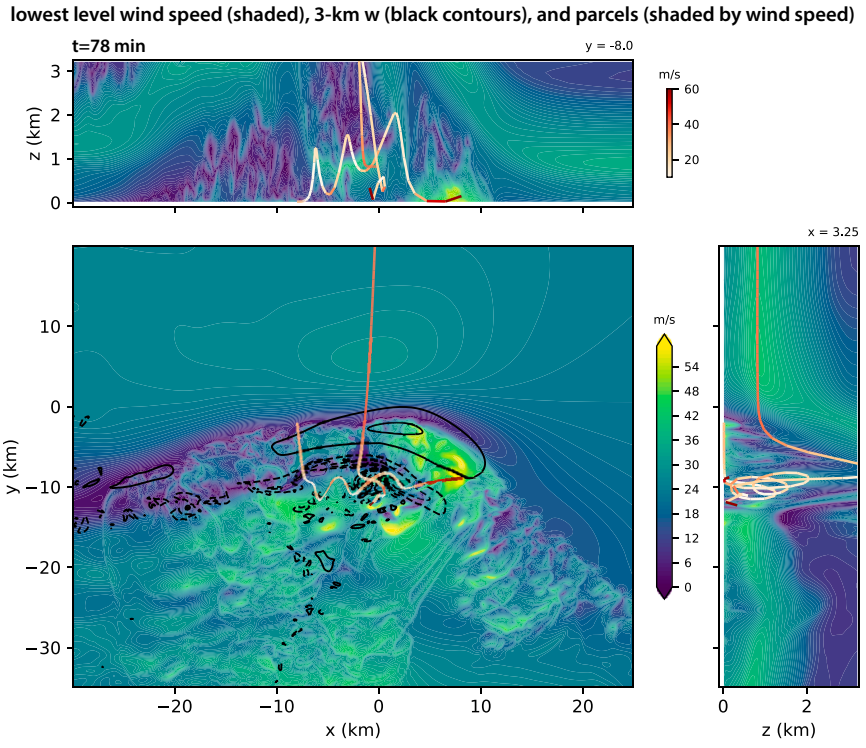

FIG. 18. Wind speed at the lowest model level (color shading, m s^{-1}), vertical velocity at 3 km (black contours every 10 m s^{-1}, zero contour omitted, negative contours dashed), and selected air parcel trajectories (shaded by wind speed) along (top) x–z, (middle) x–y, and (right) y–z planes, from the CM1 simulation at $t = 78$ min. Wind speeds in this figure are domain relative. The x and y locations used for the vertical sections are shown in the upper right of the respective panels.

in both observations and simulations were stronger than wind speeds in the layers above, highlighting the role of dynamical processes other than the downward transport of momentum. Furthermore, in the CM1 simulation, the convective line produced intense surface winds without the development of a near-surface cold pool. All of these findings point to very different mechanisms from those conventionally associated with downbursts, namely, latent cooling and hydrometeor loading.

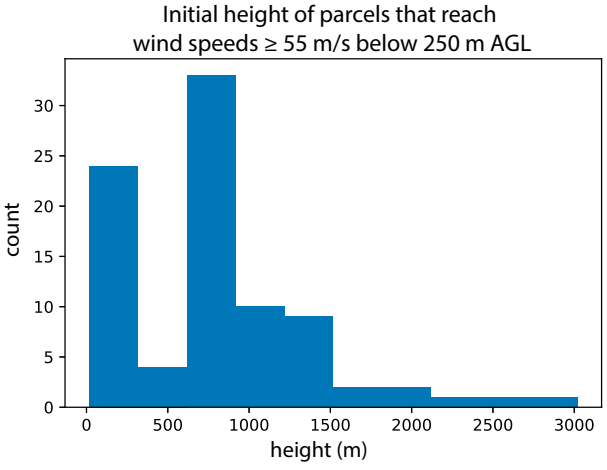

FIG. 19. Histogram of the initial height, at $t = 55$ min when parcels were initialized, of the parcels in CM1 that reached wind speeds of 55 m s^{-1} or greater in the lowest 250 m AGL. Parcels were initially evenly distributed at height levels between the surface and 4 km.

Key processes involved in the 9 June 2020 macroburst, as gleaned from the numerical simulations in this study, are summarized in Fig. 20. Air behind the surface cold front and beneath a strong inversion approaches the convective line and associated gravity wave from the north-northeast. This air ascends and decelerates in the upward branch of the wave, and the wave concurrently amplifies and eventually breaks. The wave breaking process rapidly accelerates air in the descending branch of the wave to the surface, where it produces intense winds.

It is unclear how commonly the processes described in this study occur. Whereas cold-frontal passages and strong vertical shear are commonplace in the spring and early summer in eastern Colorado, convective lines that produce destructive downbursts in the middle of the night are not. Preliminary research by Sherburn and Borchardt (2022) suggests that there have been similar events in other regions of the United States. As such, questions remain about how predictable such events are, and perhaps future research can identify additional clues to the frequency, dynamics, and predictability of downbursts connected to gravity wave breaking. Additionally, further research

Brought to you by Colorado State University Libraries | Unauthenticated | Downloaded 03/10/23 07:13 PM UTC

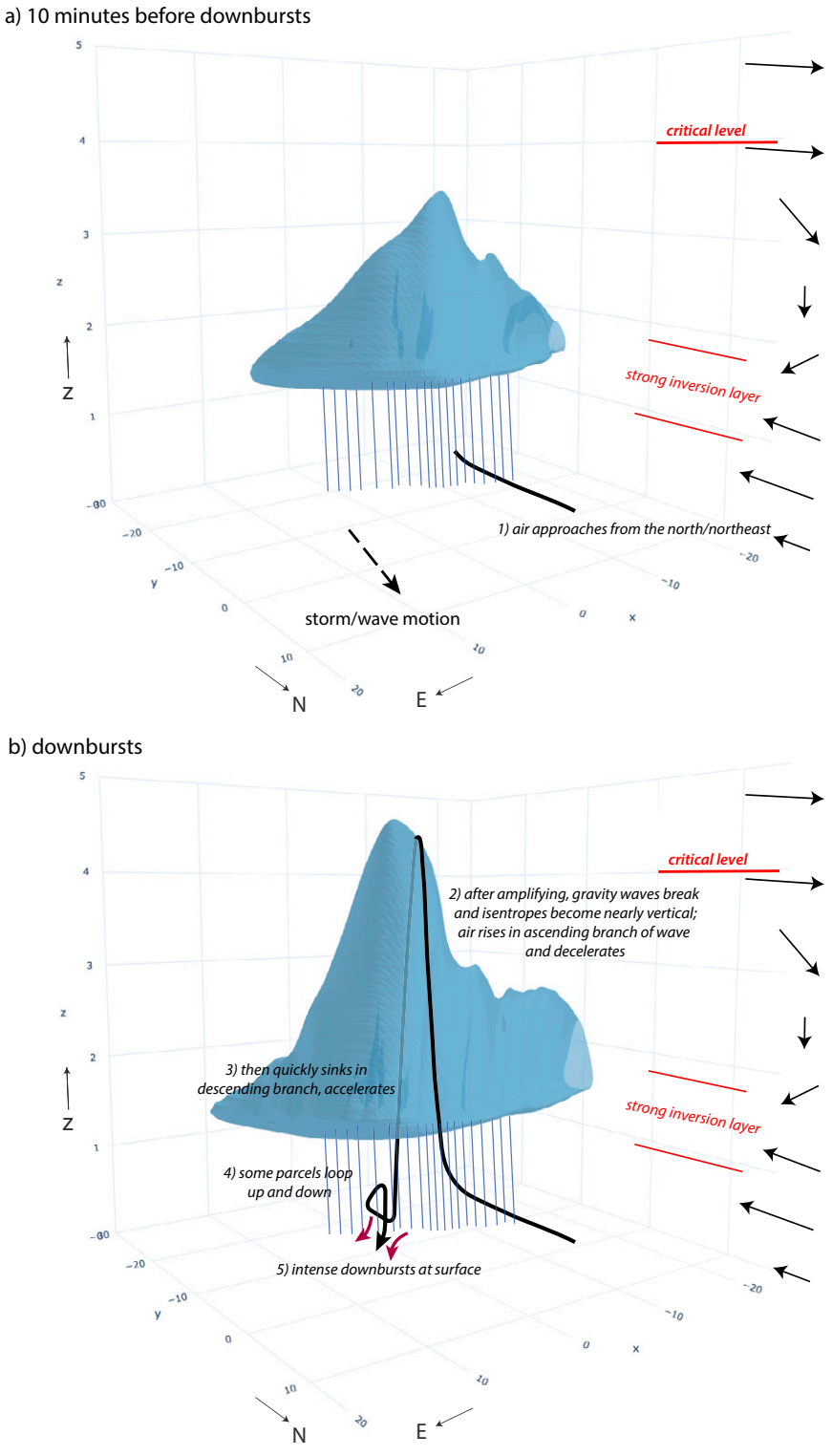

FIG. 20. Conceptual diagram of processes associated with the 9 Jun 2020 macroburst, synthesized from the WRF and CM1 simulations: (a) 10 min prior to the downbursts and (b) the approximate time of the downbursts. The blue isosurface is the −10 K potential temperature perturbation from the CM1 simulation, illustrating the gravity wave associated with the convective line. A representative parcel path, based on the parcel trajectories from both simulations, is shown with the black curve. The inversion layer and approximate vertical wind profile are shown at the right.

Brought to you by Colorado State University Libraries | Unauthenticated | Downloaded 03/10/23 07:13 PM UTC

on how such severe winds impact aviation and structures could yield new insights into how to best mitigate those impacts.

Acknowledgments. This research was supported by NSF Grants AGS-1636663 and AGS-1636667 and by the USDA National Institute of Food and Agriculture and Colorado Agricultural Experiment Station Projects COL00703B and COL00703C. The authors would like to acknowledge high-performance computing support from Cheyenne (doi:10.5065/D6RX99HX) provided by NCAR's Computational and Information Systems Laboratory, sponsored by the National Science Foundation. The authors also thank George Bryan for support of the CM1 model, and the WRF Model development team for supporting that system. The authors appreciate the constructive suggestions from three anonymous reviewers and Editor Stan Trier that led to an improved manuscript.

Data availability statement. Initialization files and namelists required to reproduce the WRF and CM1 simulations, along with the time series output, are available in the Dryad repository at https://doi.org/10.5061/dryad.44j0zpcj2. The full model output will be made available upon request to the lead author.

REFERENCES

Anabor, V., U. Rizza, E. L. Nascimento, and G. A. Degrazia, 2011: Large-eddy simulation of a microburst. *Atmos. Chem. Phys.*, **11**, 9323–9331, https://doi.org/10.5194/acp-11-9323-2011.

Atlas, D., C. W. Ulbrich, and C. R. Williams, 2004: Physical origin of a wet microburst: Observations and theory. *J. Atmos. Sci.*, **61**, 1186–1195, https://doi.org/10.1175/1520-0469(2004)061<1186:POOAWM>2.0.CO;2.

Bolgiani, P., S. Fernández-González, F. Valero, A. Merino, E. García-Ortega, J. L. Sánchez, and M. L. Martín, 2020: Simulation of atmospheric microbursts using a numerical mesoscale model at high spatiotemporal resolution. *J. Geophys. Res. Atmos.*, **125**, e2019JD031791, https://doi.org/10.1029/2019JD031791.

Bryan, G. H., and J. M. Fritsch, 2002: A benchmark simulation for moist nonhydrostatic numerical models. *Mon. Wea. Rev.*, **130**, 2917–2928, https://doi.org/10.1175/1520-0493(2002)130<2917:ABSFMN>2.0.CO;2.

Chen, F., and J. Dudhia, 2001: Coupling an advanced land surface–hydrology model with the Penn State–NCAR MM5 modeling system. Part I: Model implementation and sensitivity. *Mon. Wea. Rev.*, **129**, 569–585, https://doi.org/10.1175/1520-0493(2001)129<0569:CAALSH>2.0.CO;2.

Childs, S. J., R. S. Schumacher, and R. D. Adams-Selin, 2021: High-resolution observations of a destructive macroburst. *Mon. Wea. Rev.*, **149**, 2875–2896, https://doi.org/10.1175/MWR-D-20-0412.1.

Christie, D. R., 1989: Long nonlinear waves in the lower atmosphere. *J. Atmos. Sci.*, **46**, 1462–1491, https://doi.org/10.1175/1520-0469(1989)046<1462:LNWITL>2.0.CO;2.

Clark, T. L., and W. R. Peltier, 1977: On the evolution and stability of finite-amplitude mountain waves. *J. Atmos. Sci.*, **34**, 1715–1730, https://doi.org/10.1175/1520-0469(1977)034<1715:OTEASO>2.0.CO;2.

——, and ——, 1984: Critical level reflection and the resonant growth of nonlinear mountain waves. *J. Atmos. Sci.*, **41**, 3122–3134, https://doi.org/10.1175/1520-0469(1984)041<3122:CLRATR>2.0.CO;2.

Durran, D. R., 1990: Mountain waves and downslope winds. *Atmospheric Processes over Complex Terrain*, *Meteor. Monogr.*, No. 23, Amer. Meteor. Soc., 59–81.

——, and J. B. Klemp, 1983: A compressible model for the simulation of moist mountain waves. *Mon. Wea. Rev.*, **111**, 2341–2361, https://doi.org/10.1175/1520-0493(1983)111<2341:ACMFTS>2.0.CO;2.

Fujita, T. T., 1990: Downbursts: Meteorological features and wind field characteristics. *J. Wind Eng. Ind. Aerodyn.*, **36**, 75–86, https://doi.org/10.1016/0167-6105(90)90294-M.

Haghi, K. R., and D. R. Durran, 2021: On the dynamics of atmospheric bores. *J. Atmos. Sci.*, **78**, 313–327, https://doi.org/10.1175/JAS-D-20-0181.1.

——, D. B. Parsons, and A. Shapiro, 2017: Bores observed during IHOP_2002: The relationship of bores to the nocturnal environment. *Mon. Wea. Rev.*, **145**, 3929–3946, https://doi.org/10.1175/MWR-D-16-0415.1.

——, and Coauthors, 2019: Bore-ing into nocturnal convection. *Bull. Amer. Meteor. Soc.*, **100**, 1103–1121, https://doi.org/10.1175/BAMS-D-17-0250.1.

Helmus, J. J., and S. M. Collis, 2016: The Python ARM radar Toolkit (Py-ART), a library for working with weather radar data in the Python programming language. *J. Open Res. Software*, **4**, e25, https://doi.org/10.5334/jors.119.

Hitchcock, S. M., and R. S. Schumacher, 2020: Analysis of backbuilding convection in simulations with a strong low-level stable layer. *Mon. Wea. Rev.*, **148**, 3773–3797, https://doi.org/10.1175/MWR-D-19-0246.1.

Hjelmfelt, M. R., 1988: Structure and life cycle of microburst outflows observed in Colorado. *J. Appl. Meteor. Climatol.*, **27**, 900–927, https://doi.org/10.1175/1520-0450(1988)027<0900:SALCOM>2.0.CO;2.

Iacono, M. J., J. S. Delamere, E. J. Mlawer, M. W. Shephard, S. A. Clough, and W. D. Collins, 2008: Radiative forcing by long-lived greenhouse gases: Calculations with the AER radiative transfer models. *J. Geophys. Res.*, **113**, D13103, https://doi.org/10.1029/2008JD009944.

Janjić, Z. I., 2002: Nonsingular implementation of the Mellor-Yamada level 2.5 scheme in the NCEP Meso model. NCEP Office Note 437, 61 pp., http://www.emc.ncep.noaa.gov/officenotes/newernotes/on437.pdf.

Johns, R. H., and W. D. Hirt, 1987: Derechos: Widespread convectively induced windstorms. *Wea. Forecasting*, **2**, 32–49, https://doi.org/10.1175/1520-0434(1987)002<0032:DWCIW>2.0.CO;2.

Knupp, K., 2006: Observational analysis of a gust front to bore to solitary wave transition within an evolving nocturnal boundary layer. *J. Atmos. Sci.*, **63**, 2016–2035, https://doi.org/10.1175/JAS3731.1.

Lilly, D. K., 1978: A severe downslope windstorm and aircraft turbulence event induced by a mountain wave. *J. Atmos. Sci.*, **35**, 59–77, https://doi.org/10.1175/1520-0469(1978)035<0059:ASDWAA>2.0.CO;2.

Markowski, P., and Y. Richardson, 2010: *Mesoscale Meteorology in Midlatitudes*. Wiley-Blackwell, 430 pp.

Mellor, G. L., and T. Yamada, 1982: Development of a turbulence closure model for geophysical fluid problems. *Rev. Geophys.*, **20**, 851–875, https://doi.org/10.1029/RG020i004p00851.

Brought to you by Colorado State University Libraries | Unauthenticated | Downloaded 03/10/23 07:13 PM UTC

Morrison, H., G. Thompson, and V. Tatarskii, 2009: Impact of cloud microphysics on the development of trailing stratiform precipitation in a simulated squall line: Comparison of one- and two-moment schemes. *Mon. Wea. Rev.*, **137**, 991–1007, https://doi.org/10.1175/2008MWR2556.1.

National Weather Service, 2020: June 8–9 2020 macroburst, high wind, & mountain snow. NOAA, accessed 5 July 2022, https://www.weather.gov/bou/20200609Macroburst.

Oreskovic, C., L. G. Orf, and E. Savory, 2018: A parametric study of downbursts using a full-scale cooling source model. *J. Wind Eng. Ind. Aerodyn.*, **180**, 168–181, https://doi.org/10.1016/j.jweia.2018.07.020.

Orf, L., E. Kantor, and E. Savory, 2012: Simulation of a downburst-producing thunderstorm using a very high-resolution three-dimensional cloud model. *J. Wind Eng. Ind. Aerodyn.*, **104–106**, 547–557, https://doi.org/10.1016/j.jweia.2012.02.020.

Parker, M. D., 2021: Self-organization and maintenance of simulated nocturnal convective systems from PECAN. *Mon. Wea. Rev.*, **149**, 999–1022, https://doi.org/10.1175/MWR-D-20-0263.1.

Peltier, W. R., and T. L. Clark, 1979: The evolution and stability of finite-amplitude mountain waves. Part II: Surface wave drag and severe downslope windstorms. *J. Atmos. Sci.*, **36**, 1498–1529, https://doi.org/10.1175/1520-0469(1979)036<1498:TEASOF>2.0.CO;2.

Powers, J. G., and Coauthors, 2017: The Weather Research and Forecasting Model: Overview, system efforts, and future directions. *Bull. Amer. Meteor. Soc.*, **98**, 1717–1737, https://doi.org/10.1175/BAMS-D-15-00308.1.

Proctor, F. H., 1988: Numerical simulations of an isolated microburst. Part I: Dynamics and structure. *J. Atmos. Sci.*, **45**, 3137–3160, https://doi.org/10.1175/1520-0469(1988)045<3137:NSOAIM>2.0.CO;2.

——, 1989: Numerical simulations of an isolated microburst. Part II: Sensitivity experiments. *J. Atmos. Sci.*, **46**, 2143–2165, https://doi.org/10.1175/1520-0469(1989)046<2143:NSOAIM>2.0.CO;2.

——, 1993: Case study of a low-reflectivity pulsating microburst—Numerical simulation of the Denver, 8 July 1989, storm. Preprints, *17th Conf. on Severe Local Storms*, Saint Louis, MO, Amer. Meteor. Soc., 677–680.

Rottman, J. W., and J. E. Simpson, 1989: The formation of internal bores in the atmosphere: A laboratory model. *Quart. J. Roy. Meteor. Soc.*, **115**, 941–963, https://doi.org/10.1002/qj.49711548809.

Ruppert, J. H., Jr., S. E. Koch, X. Chen, Y. Du, A. Seimon, Y. Q. Sun, J. Wei, and L. F. Bosart, 2022: Mesoscale gravity waves and midlatitude weather: A tribute to Fuqing Zhang. *Bull. Amer. Meteor. Soc.*, **103**, E129–E156, https://doi.org/10.1175/BAMS-D-20-0005.1.

Sachsperger, J., S. Serafin, V. Grubišić, I. Stiperski, and A. Paci, 2017: The amplitude of lee waves on the boundary-layer inversion. *Quart. J. Roy. Meteor. Soc.*, **143**, 27–36, https://doi.org/10.1002/qj.2915.

Sherburn, K., and B. S. Borchardt, 2022: Elevated or not: Case studies of discrete nocturnal convection producing significant severe winds. *30th Conf. on Severe Local Storms*, Houston, TX, Amer. Meteor. Soc., 15.4B, https://ams.confex.com/ams/30SLS/meetingapp.cgi/Paper/407170.

Srivastava, R. C., 1985: A simple model of evaporatively driven downdraft: Application to microburst downdraft. *J. Atmos. Sci.*, **42**, 1004–1023, https://doi.org/10.1175/1520-0469(1985)042<1004:ASMOED>2.0.CO;2.

——, 1987: A model of intense downdrafts driven by the melting and evaporation of precipitation. *J. Atmos. Sci.*, **44**, 1752–1774, https://doi.org/10.1175/1520-0469(1987)044<1752:AMOIDD>2.0.CO;2.

Stoelinga, M. T., J. F. Bresch, P. A. Mooney, J. G. Powers, and K. W. Manning, 2018: Users' guide to RIP version 4.7: A program for visualizing mesoscale model output. Accessed 28 October 2021, https://www2.mmm.ucar.edu/wrf/users/docs/ripug.htm.

Thompson, G., P. R. Field, R. M. Rasmussen, and W. D. Hall, 2008: Explicit forecasts of winter precipitation using an improved bulk microphysics scheme. Part II: Implementation of a new snow parameterization. *Mon. Wea. Rev.*, **136**, 5095–5115, https://doi.org/10.1175/2008MWR2387.1.

van Dijke, D., Y. B. L. Hinssen, and F. Bijlsma, 2011: A 500 m WRF hindcast of a microburst event in The Netherlands. *11th EMS Annual Meeting*, Berlin, Germany, European Meteorological Society, Abstract EMS2011-546-1, https://meetingorganizer.copernicus.org/EMS2011/EMS2011-546-1.pdf.

Wakimoto, R. M., 1982: The life cycle of thunderstorm gust fronts as viewed with Doppler radar and rawinsonde data. *Mon. Wea. Rev.*, **110**, 1060–1082, https://doi.org/10.1175/1520-0493(1982)110<1060:TLCOTG>2.0.CO;2.

——, 1985: Forecasting dry microburst activity over the High Plains. *Mon. Wea. Rev.*, **113**, 1131–1143, https://doi.org/10.1175/1520-0493(1985)113<1131:FDMAOT>2.0.CO;2.

——, 2001: Convectively driven high winds. *Severe Convective Storms*, *Meteor. Monogr.*, No. 50, Amer. Meteor. Soc., 255–298, https://doi.org/10.1175/0065-9401-28.50.255.

Brought to you by Colorado State University Libraries | Unauthenticated | Downloaded 03/10/23 07:13 PM UTC